Chapter 4

Microring Resonators

4.1 Introduction

Resonators have attracted considerable attention in the area of integrated photonics. Early in 1969, microring resonators were proposed by Marcatili at Bell Labs [1]. Due to the advanced fabrication techniques, integrated microring resonators have made great progress in the last few decades. Microring resonators have many merits, compared with other kinds of resonators. First, mirrors or gratings are not needed to get optical feedback; thus, microring resonators are not so hard to fabricate and are very suitable for on-chip optical integration. Second, the microring resonator is a traveling-wave resonator, and the optical paths for input, transmission, and reflection are separated, making it very compatible with other optical components. Third, multiple microring resonators can be coupled in series or parallel to achieve a box-like response and a large free-spectrum range (FSR), making it very promising in a dense wavelength division multiplexing system.

Silicon-on-insulator (SOI) is a promising material platform for optical integration, which is low cost and compatible with complementary metal-oxide-semiconductor (CMOS) processes and has a high index contrast to obtain compact optical devices.

Silicon-Based Photonics
Erich Kasper and Jinzhong Yu

ISBN 978-981-4303-24-8 (Hardcover), 978-1-315-15651-4 (eBook)
www.jennystanford.com

Nowadays, as a basic component, the microring resonator has been widely employed to construct various optical devices, such as filters, modulators, switches, logic gates, delay lines, and sensors. For this chapter, the basic theory is illustrated in Section 4.1. Then, the optical properties and device designs are introduced in Sections 4.2 and 4.3, respectively. After that, the fabrication and measurement of the SOI-based microring resonator are presented in Section 4.4, followed by their applications in Section 4.5. Finally, we speculate about trends in silicon-based microring resonator development.

4.2 Principle of the Microring Resonator

4.2.1 Single Microring

A single microring [2–4] coupled to a bus waveguide is the simplest configuration, having an input port and an output port, as shown in Fig. 4.1a, which is equivalent to a Gires–Tournois resonator in Fig. 4.1b.

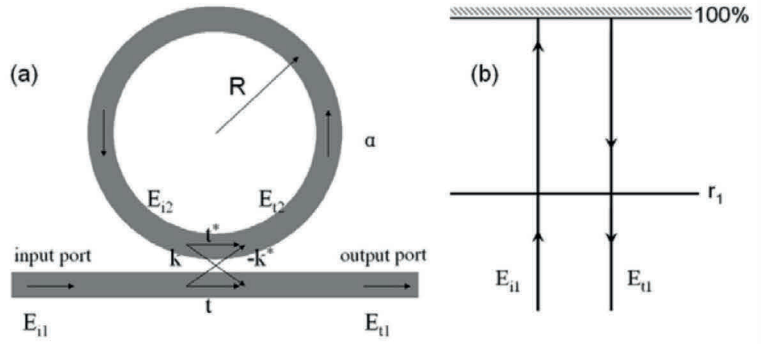

Figure 4.1 (a) Microring resonator coupled to a bus waveguide; (b) Gires–Tournois resonator.

If the waveguide has only a single mode, the coupling region is lossless, and polarization converting does not exist, we can treat all the optical loss in the ring with an attenuation factor. Then, the transfer matrix of the microring resonator can be described as

$$\begin{bmatrix} \frac{E_{t1}}{E_{t2}} \end{bmatrix} = \begin{bmatrix} t & k \\ -k^* & t^* \end{bmatrix} \begin{bmatrix} \frac{E_{i1}}{E_{i2}} \end{bmatrix} \tag{4.1}$$

where E_{t1}, E_{t2}, E_{i1}, and E_{i2} denote the optical amplitude in the positions of microring as shown in Fig. 4.1a, k is the coupling coefficient between the microring and bus waveguide, and t is the transmitting coefficient. As the coupling region is assumed lossless, k and t satisfy the following relation:

$$|k^2|+|t^2|=1 \tag{4.2}$$

After propagating in a single circle,

$$E_{i2} = \alpha e^{j\theta} E_{t2}, \tag{4.3}$$

where α is the attenuation factor in the microring, $\theta = n_{\text{eff}} L / \lambda_0$ is the phase shift in a circle, $L = 2\pi r$ is the ring perimeter, r is the ring radius, n_{eff} is the effective refractive index of the waveguide mode, and λ_0 is the optical wavelength in vacuum. According to Eq. 4.1 and Eq. 4.3, we obtain the following:

$$\frac{E_{t1}}{E_{i1}} = \frac{t - \alpha e^{j\theta}}{1 - \alpha t^* e^{j\theta}} \tag{4.4}$$

$$\frac{E_{i2}}{E_{i1}} = \frac{-\alpha k^* e^{j\theta}}{1 - \alpha t^* e^{j\theta}} \tag{4.5}$$

$$\frac{E_{t2}}{E_{i1}} = \frac{-k^*}{1 - \alpha t^* e^{j\theta}} \tag{4.6}$$

Figure 4.2a shows an add-drop filter based on a microring resonator coupled with two bus waveguides, which has four ports: input port, throughput port, add port, and drop port. This microring resonator is similar to a Fabry–Perot resonator (see Fig. 4.2b), except that the microring is a traveling-wave resonator, while Fabry–Perot is a standing-wave resonator.

With regard to the transfer function equations, Eqs. 4.4–4.6, we substitute α and t by αt_2^* and t_1, respectively, and then can obtain the transfer function at the throughput port, described by,

$$\frac{E_{t1}}{E_{i1}} = \frac{t_1 - \alpha t_2^* e^{j\theta}}{1 - \alpha t_1^* t_2^* e^{j\theta}} \tag{4.7}$$

At the drop port, the relation $E_{t2} = k_2 E_r e^{j\theta/2}$ exists.

According to Eq. 4.6, we can obtain

$$\frac{E_{t2}}{E_{i1}} = \frac{-k_1^* k_2 (\alpha e^{j\theta})^{1/2}}{1 - \alpha t_1^* t_2^* e^{j\theta}} \tag{4.8}$$

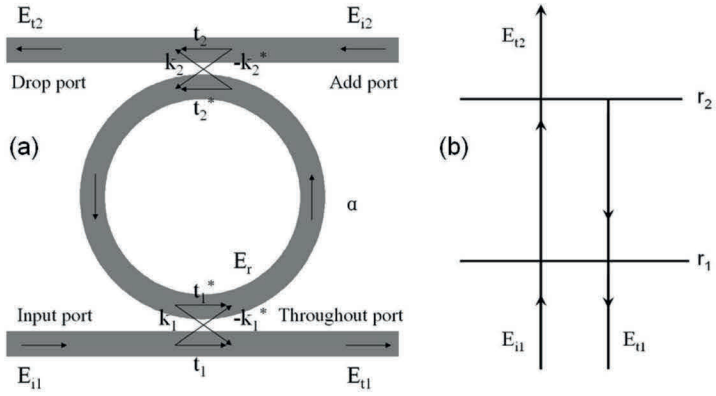

Figure 4.2 (a) Microring resonator coupled to two bus waveguides; (b) Fabry–Perot resonator.

Racetrack resonators are made with straight waveguides inserted into the coupling region to enhance the coupling efficiency between the racetrack and bus waveguides. When the coupling is very strong, the phase shift in the coupling region cannot be neglected. Thus,

$$t \to te^{j\varphi_t},\ t^* \to t^* e^{j\varphi_t},\ k \to ke^{-j\varphi_k},\ \text{and}\ k^* \to k^* e^{-j\varphi_k}.$$

Then, the transfer function at the throughput port and the drop port can be expressed as follows:

$$E_{t1} = \frac{t_1 e^{j\varphi_{t1}} - \alpha t_2^* e^{j\theta} e^{j\varphi_{t2}} (t_1 t_1^* e^{j2\varphi_{t1}} - k_1 k_1^* e^{-j2\varphi_{k1}})}{1 - \alpha t_1^* t_2^* e^{j\theta} e^{j\varphi_{t1}} e^{j\varphi_{t2}}} \tag{4.9}$$

$$E_{t2} = \frac{-\alpha^{1/2} k_1^* k_2 e^{j\theta/2} e^{-j\varphi_{k1}} e^{-j\varphi_{k2}}}{1 - \alpha t_1^* t_2^* e^{j\theta} e^{j\varphi_{t1}} e^{j\varphi_{t2}}} \tag{4.10}$$

4.2.2 Cascaded Microrings

When multiple microrings are cascaded [5, 6], the transmission becomes sophisticated. Here, the transfer matrix method has been employed to deduce the transfer functions of series-coupled microrings and parallel-coupled microrings.

4.2.2.1 Transfer matrix units

- **Directional coupler and transmission line**

For cascaded microrings, directional coupler and transmission line are basic elements having four ports, as shown in Fig. 4.3.

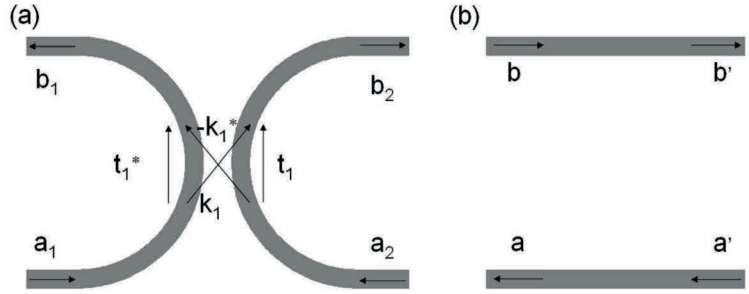

Figure 4.3 (a) directional coupler and (b) transmission line.

As seen in Fig. 4.3a, the transfer matrix equation for the directional coupler is expressed as

$$\begin{bmatrix} b_1 \\ b_2 \end{bmatrix} = \begin{bmatrix} t_1^* & -k_1^* \\ k_1 & t_1 \end{bmatrix} \begin{bmatrix} a_1 \\ a_2 \end{bmatrix}. \tag{4.11}$$

We can rewrite it as,

$$\begin{bmatrix} a_2 \\ b_2 \end{bmatrix} = \begin{bmatrix} 1/k_1 & -t_1/k_1 \\ t_1^*/k_1 & -1/k_1 \end{bmatrix} \begin{bmatrix} b_1 \\ a_1 \end{bmatrix}. \tag{4.12}$$

So, the transfer matrix P for directional coupler is expressed as

$$P = \begin{bmatrix} 1/k_1 & -t_1/k_1 \\ t_1^*/k_1 & -1/k_1 \end{bmatrix}. \tag{4.13}$$

Then, the transfer matrix equation for the transmission line in Fig. 4.3b is expressed as

$$\begin{bmatrix} b' \\ a' \end{bmatrix} = \begin{bmatrix} \alpha^{1/2}\exp(j\theta/2) & 0 \\ 0 & \alpha^{-1/2}\exp(-j\theta/2) \end{bmatrix} \begin{bmatrix} b \\ a \end{bmatrix}. \tag{4.14}$$

Also, the transfer matrix Q for the transmission line is expressed as

$$Q=\begin{bmatrix} \alpha^{1/2}\exp(j\theta/2) & 0 \\ 0 & \alpha^{-1/2}\exp(-j\theta/2) \end{bmatrix} \tag{4.15}$$

- **Microring resonator**

The microring resonator has four ports, as shown in Fig. 4.4. Using the transfer function for a microring coupled to two bus waveguides, when only a light injection in the input port or drop port is assumed, we can obtain the following expressions:

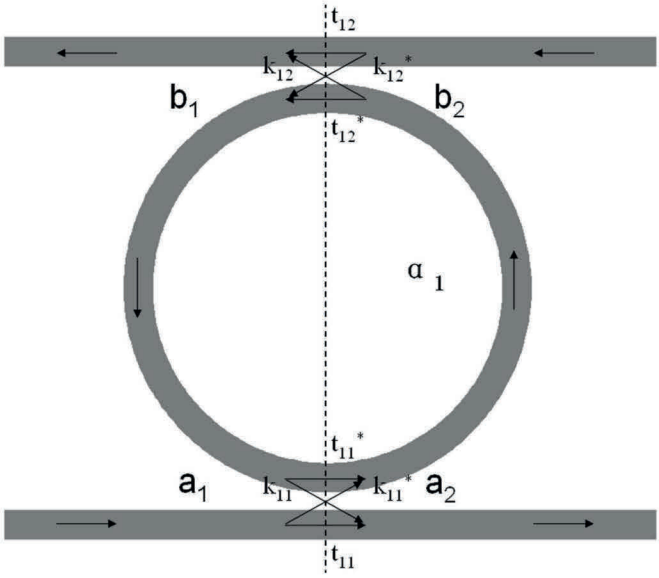

Figure 4.4 The schematic of a four-port microring resonator.

$$\tau_{11}=\frac{b_1}{a_1}=\frac{\alpha_1^{1/2}k_{11}^{*}k_{12}\exp(j\theta_1/2)}{1-\alpha_1 t_{11}^{*}t_{12}^{*}\exp(j\theta_1)} \tag{4.16}$$

$$\tau_{12}=\frac{a_2}{b_2}=\frac{\alpha_1^{1/2}k_{11}k_{12}^{*}\exp(j\theta_1/2)}{1-\alpha_1 t_{11}^{*}t_{12}^{*}\exp(j\theta_1)} \tag{4.17}$$

$$r_{11}=\frac{a_2}{a_1}=\frac{t_{11}-\alpha_1 t_{12}^{*}\exp(j\theta_1)}{1-\alpha_1 t_{11}^{*}t_{12}^{*}\exp(j\theta_1)} \tag{4.18}$$

$$r_{12} = \frac{b_1}{b_2} = \frac{t_{12} - \alpha_1 t_{11}^* \exp(j\theta_1)}{1 - \alpha_1 t_{11}^* t_{12}^* \exp(j\theta_1)} \tag{4.19}$$

When the input port and the drop port both have a light injection, then,

$$b_1 = \tau_{11} a_1 + r_{12} b_2 \tag{4.20}$$

and

$$a_2 = \tau_{12} b_2 + r_{11} a_1 . \tag{4.21}$$

Hence, we have

$$b_2 = \frac{1}{r_{12}} b_1 - \frac{\tau_{11}}{r_{12}} a_1 \tag{4.22}$$

and

$$a_2 = \frac{\tau_{12}}{r_{12}} b_1 + \frac{r_{11} r_{12} - \tau_{11} \tau_{12}}{r_{12}} a_1 . \tag{4.23}$$

So, the transfer matrix equation for a microring resonator is expressed as

$$\begin{bmatrix} b_2 \\ a_2 \end{bmatrix} = \begin{bmatrix} 1/r_{12} & -\tau_{11}/r_{12} \\ \tau_{12}/r_{12} & (r_{11} r_{12} - \tau_{11} \tau_{12})/r_{12} \end{bmatrix} \begin{bmatrix} b_1 \\ a_1 \end{bmatrix}. \tag{4.24}$$

We denote the transfer matrix for the microring resonator as *Y*.

$$Y = \begin{bmatrix} 1/r_{12} & -\tau_{11}/r_{12} \\ \tau_{12}/r_{12} & (r_{11} r_{12} - \tau_{11} \tau_{12})/r_{12} \end{bmatrix} \tag{4.25}$$

4.2.2.2 Series-coupled microring resonators

Multiple microrings are series coupled in the configuration shown in Fig. 4.5.

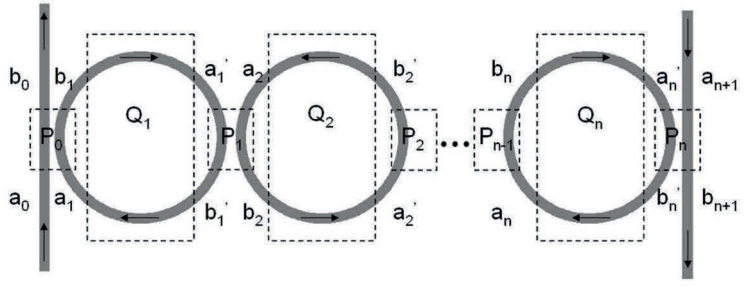

Figure 4.5 Series-coupled microring resonators.

They can be divided into multiple directional couplers and transmission lines. Therefore, the transfer matrix equation for series-coupled microring resonators can be written as

$$\begin{bmatrix} b_{n+1} \\ a_{n+1} \end{bmatrix} = P_n Q_n P_{n-1} Q_{n-1} \cdots P_1 Q_1 P_0 \begin{bmatrix} b_0 \\ a_0 \end{bmatrix} = M \begin{bmatrix} b_0 \\ a_0 \end{bmatrix}, \tag{4.26}$$

where P_n and Q_n are, respectively, described as

$$\begin{cases} P_n = \begin{bmatrix} -t/k_n & 1/k_n \\ -1/k_n & -t^*/k_n \end{bmatrix} \\ Q_n = \begin{bmatrix} 0 & \alpha_n^{1/2} \exp(j\theta_n/2) \\ \alpha_n^{-1/2} \exp(-j\theta_n/2) & 0 \end{bmatrix} \end{cases}. \tag{4.27}$$

The transfer matrix for cascaded microrings is written as

$$M = \begin{bmatrix} A & B \\ C & D \end{bmatrix}. \tag{4.28}$$

With no light injection at the add port, the transfer functions at the throughput port and the drop port can be expressed as follows:

$$\begin{cases} S_t = \dfrac{b_0}{a_0} = -\dfrac{D}{C} \\ S_d = \dfrac{b_{n+1}}{a_0} = B - \dfrac{AD}{C} \end{cases} \tag{4.29}$$

4.2.2.3 Parallel-coupled microring resonators

Figure 4.6 shows the configuration of parallel-coupled microring resonators, which can be divided into two elements, single-microring resonators and parallel transmission lines. Since there is no coupling between adjacent two microrings, the transfer matrix equation for a parallel-coupled microring can be written as

$$\begin{bmatrix} b_n \\ a_n \end{bmatrix} = Y_n X_{n-1} Y_{n-1} X_{n-2} \cdots Y_2 X_1 Y_1 \begin{bmatrix} b_0 \\ a_0 \end{bmatrix} = N \begin{bmatrix} b_0 \\ a_0 \end{bmatrix}, \tag{4.30}$$

where the transfer matrixes for the microring and the transmission line are expressed as

$$Y_n = \begin{bmatrix} 1/r_{n2} & -\tau_{n1}/r_{n2} \\ \tau_{n2}/r_{n2} & (r_{n1}r_{n2} - \tau_{n1}\tau_{n2})/r_{n2} \end{bmatrix} \tag{4.31}$$

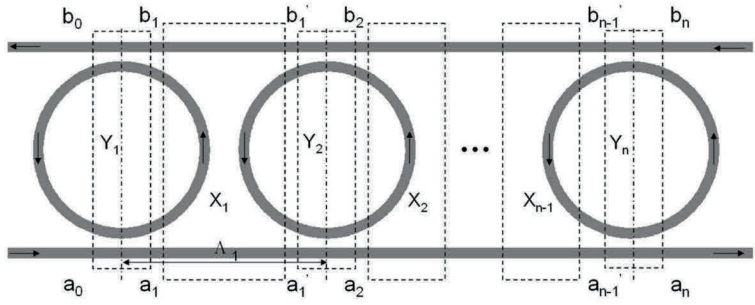

Figure 4.6 Parallel-coupled microring resonators.

and

$$X_n = \begin{bmatrix} \alpha_n^{1/2} \exp(j\theta_n') & 0 \\ 0 & \alpha_n^{-1/2} \exp(-j\theta_n') \end{bmatrix}, \tag{4.32}$$

where $\theta_n' = \beta\Lambda_n$.

The transfer matrix N for cascaded microrings is specified by

$$N = \begin{bmatrix} E & F \\ G & H \end{bmatrix}.$$

Therefore, the transfer function for the parallel-coupled microrings at the throughput port and the drop port can be expressed by:

$$S_t = \frac{a_n}{a_0} = H - \frac{FG}{E} \tag{4.33}$$

$$S_d = \frac{b_0}{a_0} = -\frac{F}{E} \tag{4.34}$$

Microring resonators can construct various functional devices with other optical components, for which transfer functions can be obtained using the transfer matrix method. First, we divide the complicated configuration into basic elements, such as directional coupler, transmission line, and microring resonator. Then, with their transfer matrixes employed, the transfer function for the aimed configuration can be derived.

4.3 Optical Properties of Microring Resonators

4.3.1 Properties of Amplitude

4.3.1.1 Single microring

- **Transmission spectrum**

Set the input optical intensity as 1; then the output optical intensities at the throughput port and the drop port are described as follows:

$$\left|E_{t1}\right|^2 = \frac{\left|t_1\right|^2 + \alpha^2\left|t_2\right|^2 - 2\alpha\left|t_1 t_2\right|\cos(\theta + \varphi_{t1} + \varphi_{t2})}{1 + \alpha^2\left|t_1 t_2\right|^2 - 2\alpha\left|t_1 t_2\right|\cos(\theta + \varphi_{t1} + \varphi_{t2})} \tag{4.35}$$

and

$$\left|E_{t2}\right|^2 = \frac{\alpha\left|k_1 k_2\right|^2}{1 + \alpha^2\left|t_1 t_2\right|^2 - 2\alpha\left|t_1 t_2\right|\cos(\theta + \varphi_{t1} + \varphi_{t2})}, \tag{4.36}$$

where t_1 and t_2 are the transmitting coefficients and φ_{t1} and φ_{t2} are the phase shifts in the coupling-in region and coupling-out region, respectively. When $\theta + \varphi_{t1} + \varphi_{t2} = 2m\pi$ (m is an integer) is satisfied, the microring is resonating and also has

$$\left|E_{t1}\right|^2 = \frac{\left(\left|t_1\right| - \alpha\left|t_2\right|\right)^2}{\left(1 - \alpha\left|t_1 t_2\right|\right)^2} \tag{4.37}$$

and

$$\left|E_{t2}\right|^2 = \frac{\alpha(1 - \left|t_1\right|^2)(1 - \left|t_2\right|^2)}{\left(1 - \alpha\left|t_1 t_2\right|\right)^2} \tag{4.38}$$

Figure 4.7 plots the transmission spectrum of the microring resonator. The throughput port outputs most of the light in the case of off-resonance, while the drop port outputs most of the light in the case of on-resonance. At $|t_1| = \alpha|t_2|$, called the critical coupling condition, no light is transmitted to the throughput port and the optical intensity at the drop port achieves the maximum when the microring is resonating.

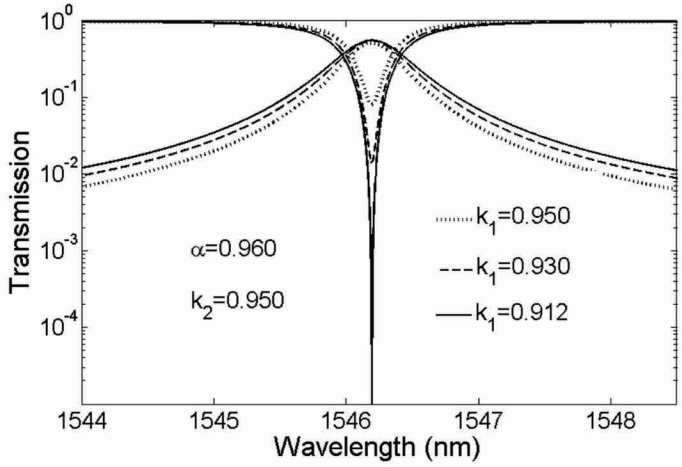

Figure 4.7 The transmission spectrum of the microring resonator.

- **Performance parameters**

The main parameters to characterize microring resonators are the FSR, quality factor, the extinction ratio (ER), and the intensity enhancement (IE) [7]. Figure 4.8 shows the transmission spectrum of the microring add-drop filter with these parameters labeled.

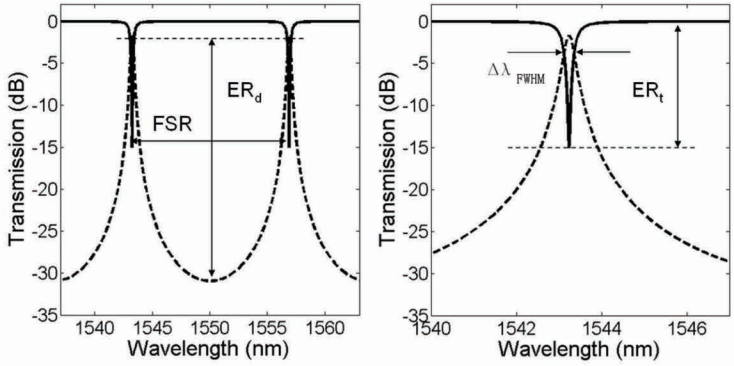

Figure 4.8 The transmission spectrum of a microring add-drop filter.

The FSR represents the spacing between two adjacent peaks in the transmission of a microring resonator, and it depends on the

propagation constant dispersion.

$$\frac{\partial\beta}{\partial\lambda}=\frac{\partial(2\pi n_{\text{eff}}/\lambda)}{\partial\lambda}=\frac{\beta}{\lambda}+k\frac{\partial n_{\text{eff}}}{\partial\lambda} \tag{4.39}$$

Assume that the optical dispersion is weak; thus, we have $\partial\beta/\partial\lambda\approx-(\beta/\lambda)$ and then

$$\text{FSR}=-\frac{2\pi}{L}\left(\frac{\partial\beta}{\partial\lambda}\right)^{-1}\approx\frac{\lambda^2}{n_{\text{eff}}L} \tag{4.40}$$

However, this assumption brings a large error when the optical dispersion is strong. The group index n_g is specified by

$$n_g=\frac{\lambda}{k}\cdot\frac{\partial\beta}{\partial\lambda}=n_{\text{eff}}-\lambda\frac{\partial n_{\text{eff}}}{\partial\lambda} \tag{4.41}$$

So, the FSR is

$$\text{FSR}=-\frac{2\pi}{L}\left(\frac{\partial\beta}{\partial\lambda}\right)^{-1}\approx\frac{\lambda^2}{n_gL} \tag{4.42}$$

The quality factor Q is the ratio of power storage and power dissipation, and it is equal to the ratio of resonant wavelength and full width at half maximum. According to the transfer function of the microring add-drop filter, we can obtain

$$\left|\frac{-k_1^*k_2(\alpha e^{j\theta})^{1/2}}{1-\alpha t_1^*t_2^*e^{j\theta}}\right|^2=\frac{\alpha|k_1|^2|k_2|^2}{2(1-\alpha|t_1t_2|)^2}. \tag{4.43}$$

There is no extra loss and a minor phase shift in the coupling region. Hence,

$$\frac{\alpha k_1^2k_2^2}{1-2\alpha t_1t_2\cos(\Delta\theta)+(\alpha t_1t_2)^2}=\frac{\alpha k_1^2k_2^2}{2(1-\alpha t_1t_2)^2}. \tag{4.44}$$

When $\Delta\theta$ is very small, we can get $\cos(\Delta\theta)=1-\frac{(\Delta\theta)^2}{2}$ and $\Delta\theta=\frac{(1-\alpha t_1t_2)^2}{\alpha t_1t_2}$.

The quality factor can be expressed as

$$Q=\frac{\omega_0}{2\Delta\omega}=\frac{(2\pi c/\lambda_0)}{2\Delta\theta c/(n_{\text{eff}}L)}=\frac{\pi n_{\text{eff}}L}{\lambda_0\Delta\theta}. \tag{4.45}$$

Therefore, the quality factor is

$$Q = \frac{\pi n_{\text{eff}} L}{\lambda_0} \cdot \frac{\sqrt{\alpha t_1 t_2}}{1 - \alpha t_1 t_2} . \tag{4.46}$$

The ER determines the depth of resonant peaks, which is equal to the ratio of maximum power and minimum power at the output port.

The output power at the throughput port is

$$\left|E_{t1}\right|^2 = \frac{t_1^2 + \alpha^2 t_2^2 - 2\alpha t_2 \cos\theta}{1 + \alpha^2 t_1^2 t_2^2 - 2\alpha t_1 t_2 \cos\theta} . \tag{4.47}$$

Then, the extinction ratio is

$$ER_t = \frac{\left|E_{t1}\right|^2_{\max}}{\left|E_{t1}\right|^2_{\min}} = \frac{\left|E_{t1}\right|^2_{\cos\theta=1}}{\left|E_{t1}\right|^2_{\cos\theta=-1}} = \frac{(t_1 - \alpha t_2)^2}{(1 - \alpha t_1 t_2)^2} - \frac{(1 + \alpha t_1 t_2)^2}{(t_1 + \alpha t_2)^2} . \tag{4.48}$$

Similarly, we can get the extinction ratio at the drop port

$$ER_{\text{d}} = \frac{(1 + \alpha t_1 t_2)^2}{(1 - \alpha t_1 t_2)^2} \tag{4.49}$$

The IE is the ratio of optical power in the resonator and that in the bus waveguides. For the microring add-drop filter, the optical power in the microring satisfies

$$\frac{E_{t2}}{E_{i1}} = \frac{-k_1^*}{1 - \alpha t_1^* t_2^* e^{j\theta}} . \tag{4.50}$$

The power in the microring is considered to be uniform; then, the intensity enhancement is

$$\text{IE} = \left|\frac{E_{t2}}{E_{i1}}\right|^2_{\phi=0} = \frac{k^2}{1 + \alpha^2 t_1^2 t_2^{\,2} - 2\alpha t_1 t_2} . \tag{4.51}$$

When $k_1 = k_2 = k$ and $k < 1$, we have IE $\approx k^2$.

4.3.1.2 Cascaded microrings

- **Optical filter with a box-like response**

The ideal response is shaped like a box for optical filters used in the wavelength division multiplexing system. The Butterworth

filter has the flattest pass-band and stop-band, while the Chebyshev filter has the sharpest band edge and small waviness in the pass-band or the stop-band [2]. With some conditions satisfied, cascaded microrings have a better response than a single microring. Table 4.1 gives the necessary conditions for cascaded microrings to construct a Butterworth filter and a Chebyshev filter.

Table 4.1 The necessary conditions for Butterworth and Chebyshev filters

N	Butterworth filter	Chebyshev filter
2	$\mu_1^{*2} = 0.250\mu^{*4}$	$\mu_1^{*2} = 0.250\mu^{*4}(1+2y)$
3	$\mu_1^{*2} = \mu_1^{*2} = 0.125\mu^{*4}$	$\mu_1^{*2} = \mu_2^{*2} = 0.125\mu^{*4}(1+1.5y^{2/3})$
4	$\mu_1^{*2} = \mu_3^{*2} = 0.100\mu^{*4}$ $\mu_2^{*2} = 0.040\mu^{*4}$	
5	$\mu_1^{*2} = \mu_4^{*2} = 0.0955\mu^{*4}$ $\mu_2^{*2} = \mu_3^{*2} = 0.040\mu^{*4}$	
6	$\mu_1^{*2} = \mu_5^{*2} = 0.0915\mu^{*4}$ $\mu_2^{*2} = \mu_4^{*2} = 0.0245\mu^{*4}$ $\mu_3^{*2} = 0.0179\mu^{*4}$	

The waviness in the pass-band of the Chebyshev filter is determined by y in Table 4.1, where μ_n and μ are

$$\mu_n^2 = k_n^2 \frac{v_{gn} v_{gn+1}}{(2\pi R_n)(2\pi R_{n+1})} \tag{4.52}$$

and

$$\mu^2 = k^2 \frac{v_{g1}}{2\pi R_1}. \tag{4.53}$$

In the expressions above, k_n is the coupling coefficient between ring n and ring $n + 1$, k is the coupling coefficient between ring and bus waveguide, and R_n and v_{gn} are the radius and group velocity

of the guided mode in ring n. Figure 4.9 plots the transmission of a single ring, cascaded double rings, and cascaded triple rings. One notices that the pass-band becomes flat and the band edge becomes sharp, as the number of microrings increases.

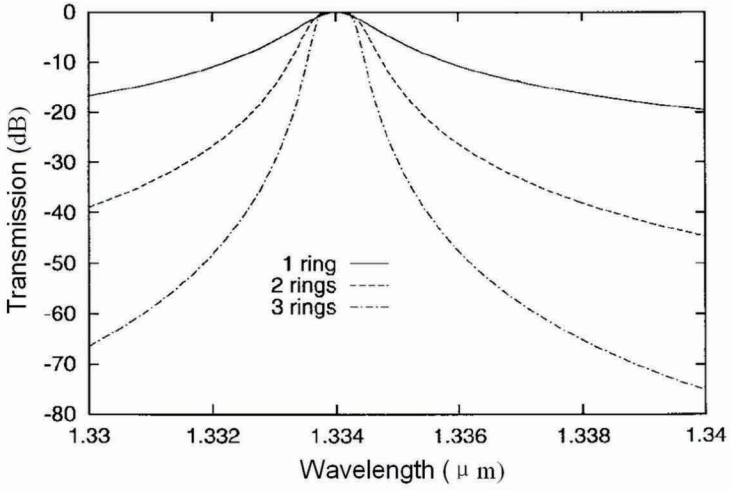

Figure 4.9 The transmissions of a single ring and cascaded microrings.

- **The Vernier effect**

The cascaded microring resonators show the Vernier effect [8] when their radii are different.

Take coupled double microrings as an example, shown in Fig. 4.10a; the light tunnels to the output port only when both microrings are resonating. Hence, the FSR of double-coupled microrings satisfies

$$\mathrm{FSR}_{12} = N_1 \cdot \mathrm{FSR}_1 = N_2 \cdot \mathrm{FSR}_2, \tag{4.54}$$

where FSR_1, FSR_2, and FSR_{12} are the FSRs of ring 1, ring 2, and coupled double rings, respectively. Both N_1 and N_2 are integers. Figure 4.10b shows the output transmissions of the individual ring and coupled rings. We find that the FSR is enlarged when the ring radii are different.

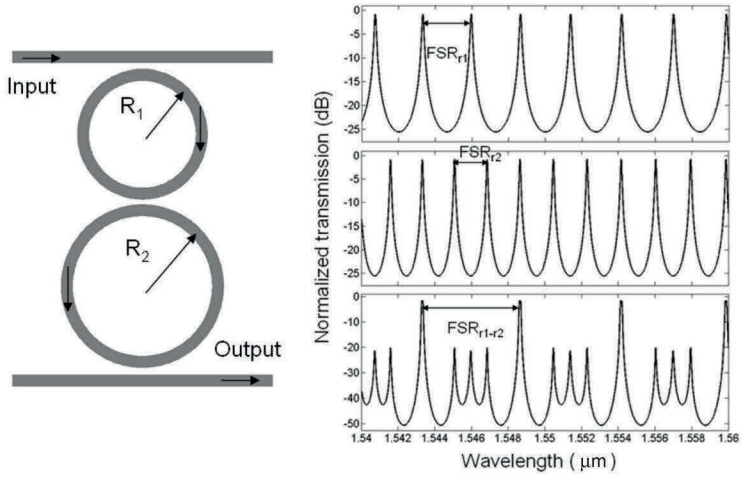

Figure 4.10 (Left) Series-coupled double microrings with different radii and (right) the Vernier effect of cascaded microrings. © 2002 IEEE. Reprinted, with permission, from Ref. [8].

4.3.2 Properties of Phase

As the optical phase is sensitive to wavelength, the light would be slowed or accelerated by microring resonators [9]. Therefore, it is promising for a microring resonator to act as an optical buffer in an optical interconnect system.

The optical phase from an all-pass filter based on a single microring is expressed as

$$\frac{E_t}{E_i} = \exp[j(\pi+\theta)]\frac{\alpha - t\exp(-j\theta)}{1-\alpha t\exp(j\theta)} \tag{4.55}$$

and

$$\begin{aligned}\Phi &= \arg\left(\frac{E_t}{E_i}\right) \\ &= \pi + \theta + \arctan\left(\frac{t\sin\theta}{\alpha - t\cos\theta}\right) + \arctan\left(\frac{\alpha t\sin\theta}{1-\alpha t\sin\theta}\right).\end{aligned} \tag{4.56}$$

For an add-drop filter based on a single microring, the throughput optical phase is

$$\frac{E_{t1}}{E_{i1}} = \exp[j(\pi+\theta)]\frac{\alpha t_2 - t_1\exp(-j\theta)}{1-\alpha t_1 t_2\exp(j\theta)} \tag{4.57}$$

and

$$\Phi = \arg\left(\frac{E_{t1}}{E_{i1}}\right)$$

$$= \pi + \theta + \arctan\left(\frac{t_1 \sin\theta}{\alpha t_2 - t_1 \cos\theta}\right) + \arctan\left(\frac{\alpha t_1 t_2 \sin\theta}{1 - \alpha t_1 t_2 \cos\theta}\right) \quad (4.58)$$

and the drop optical phase is

$$\frac{E_{t2}}{E_{i1}} = \frac{k_1 k_2 [\alpha \exp(i\theta)]^{1/2}}{1 - \alpha t_1 t_2 \exp(i\theta)} \quad (4.59)$$

and

$$\Phi = \arg\left(\frac{E_{t2}}{E_{i1}}\right) = \frac{\theta}{2} + \arctan\left(\frac{\alpha t_1 t_2 \sin\theta}{1 - \alpha t_1 t_2 \cos\theta}\right). \quad (4.60)$$

The curves in Fig. 4.11 show the optical phases from the microring add-drop filter as a function of the wavelength when there is undercoupling ($t_1 > t_2$), symmetric coupling ($t_1 = t_2$), or overcoupling ($t_1 < t_2$). The resonance wavelength is chosen at about 1.55 μm. At the throughput port, the phase jumps at the resonance frequency whereas the phase increases monotonically at the drop port.

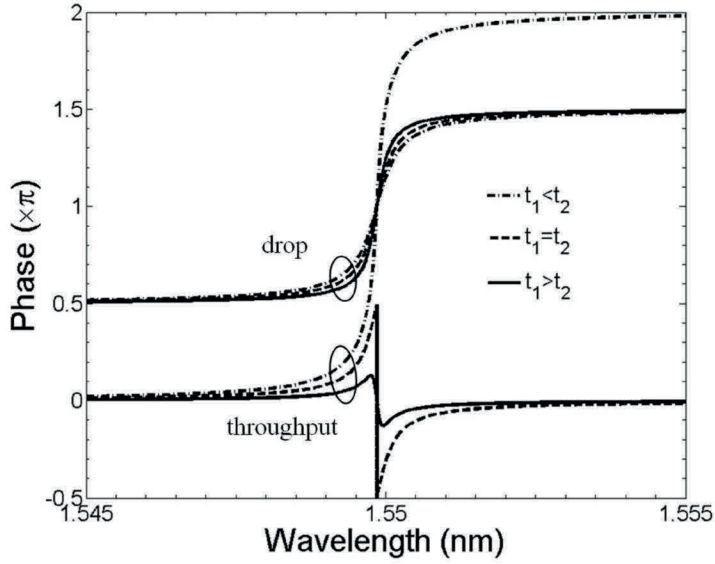

Figure 4.11 The phase curves at the throughput port and the drop port for a microring add-drop filter.

To get slow light or fast light, we have to change the optical group velocity through structure dispersion or material dispersion. The group velocity of light is described by

$$v_g = \frac{\partial \omega}{\partial k} = \frac{c - \omega \dfrac{\partial n(\omega,k)}{\partial k}}{n(\omega,k) + \omega \dfrac{\partial n(\omega,k)}{\partial \omega}}. \tag{4.61}$$

A microring resonator can slow down the light through structure dispersion. As seen in Fig. 4.12, the optical pulse of the Gaussian shape is delayed for picoseconds, reflecting that the microring resonator captures, stores, and then releases the light. Note that the pulse width should be comparable with the lifetime in the resonator, as otherwise, the output pulse would be distorted.

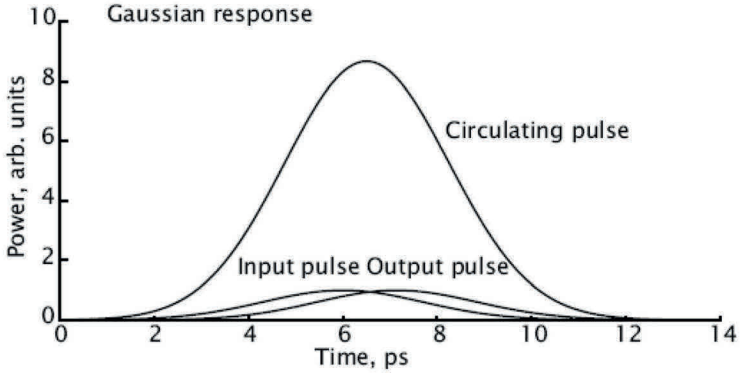

Figure 4.12 The time delay of the optical pulse in the Gaussian shape.

The time delay is denoted by

$$\tau_d = -\frac{d\Phi}{d\theta} \cdot \frac{d\theta}{d\omega} \text{ and } \frac{d\theta}{d\omega} = \frac{n_g L}{c}. \tag{4.62}$$

For a microring all-pass filter

$$\frac{d\Phi}{d\theta} = \frac{\alpha^2 - \alpha t \cos\theta}{\alpha^2 + t^2 - 2\alpha t \cos\theta} + \frac{\alpha t \cos\theta - \alpha^2 t^2}{1 + \alpha^2 t^2 - 2\alpha t \cos\theta}, \tag{4.63}$$

Therefore,

$$\tau_d = -\left(\frac{\alpha^2 - \alpha t \cos\theta}{\alpha^2 + t^2 - 2\alpha t \cos\theta} + \frac{\alpha t \cos\theta - \alpha^2 t^2}{1 + \alpha^2 t^2 - 2\alpha t \cos\theta} \right) \cdot \frac{n_g L}{c} \tag{4.64}$$

For the throughput port of the microring add-drop filter

$$\frac{d\Phi}{d\theta}=\frac{\alpha^2t_2^2-\alpha t_1t_2\cos\theta}{\alpha^2t_2^2+t_1^2-2\alpha t_1t_2\cos\theta}+\frac{\alpha t_1t_2\cos\theta-\alpha^2t_1^2t_2^2}{1+\alpha^2t_1^2t_2^2-2\alpha t_1t_2\cos\theta} \tag{4.65}$$

and

$$\tau_{\mathrm{d}}=-\left(\frac{\alpha^2t_2^2-\alpha t_1t_2\cos\theta}{\alpha^2t_2^2+t_1^2-2\alpha t_1t_2\cos\theta}+\frac{\alpha t_1t_2\cos\theta-\alpha^2t_1^2t_2^2}{1+\alpha^2t_1^2t_2^2-2\alpha t_1t_2\cos\theta}\right)\cdot\frac{n_{\mathrm{g}}L}{c}. \tag{4.66}$$

For the drop port of the microring add-drop filter

$$\frac{d\Phi}{d\theta}=\frac{1}{2}+\frac{\alpha t_1t_2\cos\theta-\alpha^2t_1^2t_2^2}{1+\alpha^2t_1^2t_2^2-s2\alpha t_1t_2\cos\theta} \tag{4.67}$$

and

$$\tau_{\mathrm{d}}=-\left(\frac{1}{2}+\frac{\alpha t_1t_2\cos\theta-\alpha^2t_1^2t_2^2}{1+\alpha^2t_1^2t_2^2-2\alpha t_1t_2\cos\theta}\right)\cdot\frac{n_{\mathrm{g}}L}{c}. \tag{4.68}$$

We can conclude from Fig. 4.13 that slow light or fast light achieves the maximum at the resonant wavelength. When it is undercoupling ($t_1 > t_2$), light is speeded at the throughput port, while it is slowed at the drop port. When it is symmetrical coupling ($t_1 = t_2$), no light is observed at the throughput port, while light is slowed at the drop port. When it is overcoupling ($t_1 < t_2$), light is slowed both at the throughput port and the drop port.

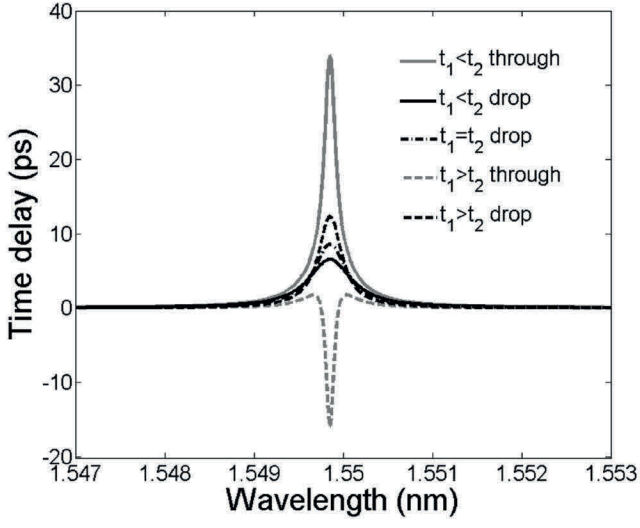

Figure 4.13 The slow light and fast light of a microring add-drop filter.

4.4 Design of Microring Resonators

Microring resonators can be characterized by transfer functions, which are mainly influenced by guided modes in waveguide, coupling efficiency, and internal loss. First, we calculate such parameters for the designed structure and then substitute them into the transfer function; thus, we can simulate the response of the microring resonator, which is much faster than a full numerical method. In this section, we will introduce the design course for including submicron waveguide, directional coupler, and internal loss in the microring.

4.4.1 Waveguide Design

- **Single-mode condition**

The waveguides in microring resonators should have a single guided mode. The properties of guided modes are determined by the waveguide structure, such as width, height, and etching depth. As dimensions are scaled down, the single-mode condition for submicron waveguides becomes different from the traditional single-mode condition [10], as shown in Fig. 4.14. It is found that rib waveguides still support a single mode with the ratio of rib height

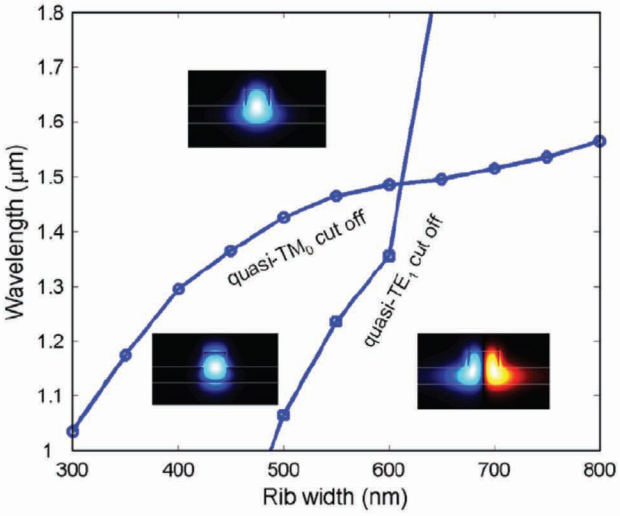

Figure 4.14 The mode cut-off condition for submicron SOI waveguides. Reprinted from Ref. [10], Copyright (2009), with permission from Elsevier.

to slab height lower than 0.5. Moreover, the transverse-magnetic mode is no longer guided in the waveguide of shallow-etched ribs since it is more likely to leak from the slab as the waveguide width decreases. The properties of bent waveguides are similar to those of straight waveguides. However, the mode profile lies outside the middle of the waveguide and radiation loss cannot be neglected for bent waveguides.

- **Polarization independence**

The index and stress profiles are anisotropic for waveguides with an asymmetric cross section, making rather large differences between transverse-electric mode and transverse-magnetic mode, especially for submicron waveguides, as seen in Fig. 4.15. The main solutions for reducing polarization dependence are:

- o Optimizing the etching depth and waveguide width to realize polarization independence
- o Tuning the thickness and strain of oxide cladding to realize polarization independence by introducing material stress

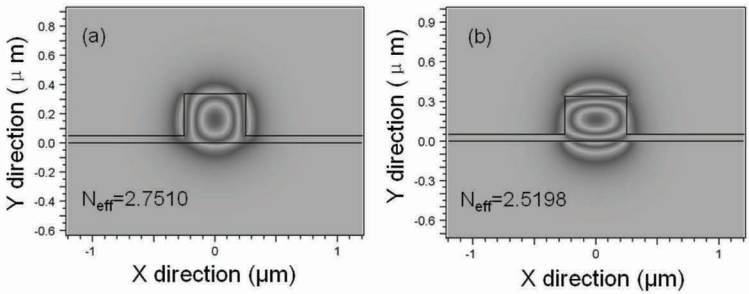

Figure 4.15 The TE mode (a) and TM mode (b) of a rib waveguide.

However, both these methods demand high-accuracy fabrication techniques. Another method is using polarization converters to make the subsystem polarization entirely independent while the microring resonators are still polarization dependent partially [11].

4.4.2 Coupler Design

The microring and microring/straight waveguide are usually coupled using a directional coupler or multimode interferometer

(MMI). The fabrication tolerance for the MMI is relatively large, while the splitting ratio is inflexible and the insertion loss is large. On the contrary, the splitting ratio is flexible and the insertion loss is low for a directional coupler. Here, we focus on the directional coupler.

The spacing is changing for the bent coupling [12], as shown in Fig. 4.16, where R denotes the ring radius and the gap denotes the minimum spacing. Suppose the dimensions of coupled waveguides are identical, and they are far smaller than the ring radius. Then, the phase mismatch and the optical loss in the coupling region can be neglected. Therefore, the transmitting coefficient t and coupling k are expressed as follows:

$$t = \cos\left(\int_{-L}^{L} k(z)dz\right),\ k = \sin\left(\int_{-L}^{L} k(z)dz\right), \tag{4.69}$$

where $k(z)$ is the coupling coefficient as a function of position in the z direction. As the coupling is angled, it should be revised by $k(z) = k_{||}(z) \cos \theta$, where $k_{||}(z)$ is the parallel coupling coefficient and it is given by

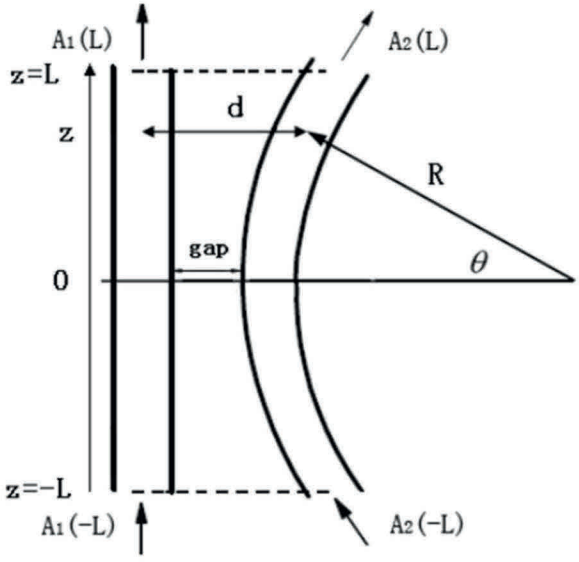

Figure 4.16 The coupling between a bent waveguide and a straight waveguide.

$$k_{\parallel}[d(z)] = \frac{i\omega\varepsilon_0}{4}\int_{-\infty}^{\infty}(n_1^2 - n_2^2)E_1^*(x)\cdot E_2(x)dx, \tag{4.70}$$

where n_1 and n_2 are indexes of core and cladding, respectively; $E_1{}^*(x)$ and $E_2(x)$ are the optical field profiles in two waveguides; ω is the optical angle frequency; and ε_0 is the dielectric constant in vacuum.

To deal with the coupling of 3D waveguides, such as rib waveguides and strip waveguides, we have to transform them into 2D slab waveguides using the effective index method at first. The coupling efficiency is influenced by the following factors: rib width, rib height, slab height, bending radius, and spacing gap. As shown in Fig. 4.17, the coupling efficiency can be enhanced by decreasing the rib width/height ratio or increasing the slab height, which may weaken the optical constraint in waveguides. By narrowing the spacing, enlarging the bending radius, or lengthening the coupling region, we can enhance the coupling greatly. For a given geometry, it is found that the coupling efficiency increases with wavelength.

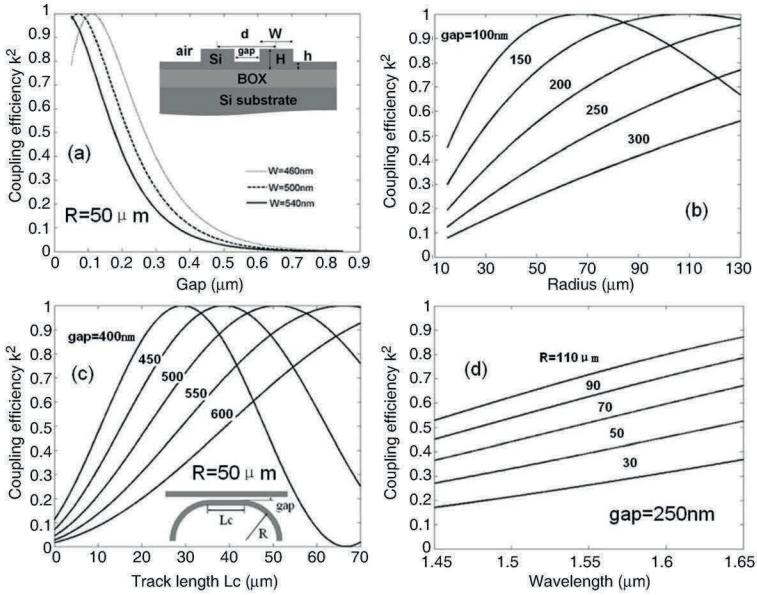

Figure 4.17 Coupling of ridge waveguides. (a) Coupling efficiency versus gap; inset: the cross section of the coupling region; (b) coupling efficiency versus bending radius; (c) coupling efficiency versus track length; (d) coupling efficiency versus wavelength.

4.4.3 Internal Loss

The absorption coefficient is very small for bulk silicon, and generally, the optical nonlinear effects are very weak. Therefore, the total optical absorption can be neglected in SOI waveguides. In reality, the internal loss mainly comes from bending loss and scattering loss.

- **Bending loss**

A simple method to calculate bending loss is proposed by Marcuse [13], from which we first transform the 3D waveguides into slab waveguides using the effective index method and then calculate the bending loss based on slab waveguides by using the following expressions [14]:

$$\alpha_{\text{bend}} = \frac{\alpha_y^2}{k_0^3(1+\alpha_y w/2)}\frac{k_y^2}{(n_{e2}^2 - n_{e1}^2)}\exp(\alpha_y w)\exp\left(\frac{-2\alpha_y^3}{3n_e^2 k_0^2}R\right) \quad (4.71)$$

and

$$\text{Loss}_{\text{bend}} = -10\log_{10}(\exp(-\alpha_{\text{bend}}\Delta\theta R)) \quad (4.72)$$

where $\alpha_y = k_0(n_e^2 - n_{e1}^2)^{1/2}$, $k_y = k_0(n_{e2}^2 - n_e^2)^{1/2}$, $k_0 = 2\pi/\lambda_0$, and α_{bend} are the imaginary parts of the propagation constant, denoting the bending loss, n_e is the effective index of the fundamental mode, n_{e1} is the effective index of the outer slab region, and n_{e2} is the effective index of the inner slab region.

Figure 4.18 shows the bending loss of the 90° curvature for SOI rib waveguides, with a rib height of 0.34 μm and an etching depth of

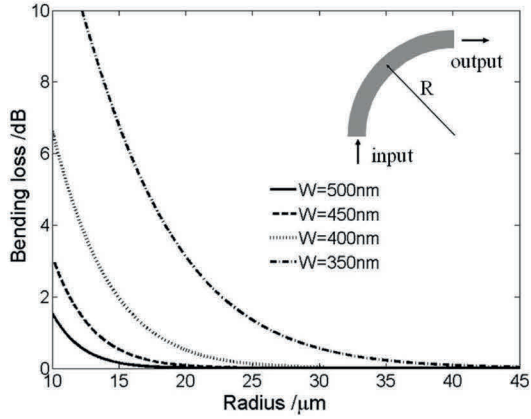

Figure 4.18 Bending loss versus bending radius.

0.17 μm, according to Eqs. 4.71–4.72. It is obvious that the bending loss rises rapidly with the bending radius and almost no bending loss exists for bending radii larger than 40 μm.

Bending loss is influenced not only by radius but also by the optical constraint in waveguides. Generally, the smaller the mode profile, the smaller is the radiation loss. Therefore, an effective method to reduce bending loss is enlarging the bending radius or increasing the etching depth.

- **Scattering loss**

The internal total reflecting model [15, 16] can explain the scattering loss. The roughness at the boundaries causes optical scattering when the light reflects between the upper and lower interfaces as propagating. The rougher the surface, the larger is the scattering loss, especially when the intensity at the interface is large.

On the basis of the Raleigh scattering theory, Tien presented an optical scattering model [16], suitable for asymmetric slab waveguides, and the power attenuation can be evaluated by

$$\alpha = K^2 \left(\frac{\cos^3 \theta}{2 \sin \theta} \right) \left\{ \frac{1}{[t + (1/p_{10}) + (1/p_{12})]} \right\}, \tag{4.73}$$

where $K = (4\pi/\lambda)(\sigma_{12}^2 + \sigma_{12}^2 + \sigma_{10}^2)^{1/2}$, θ is the light transmitting angle, λ is the optical wavelength in waveguides, t is the waveguide thickness, and $1/p_{10}$ and $1/p_{12}$ are the depths of light in cladding and substrate, respectively. In addition, σ_{10} and σ_{12} are the mean square roots of roughness in cladding and substrate, respectively.

The scattering loss is proportional to the roughness and the square of index contrast at the boundaries. It is found that the scattering loss mainly comes from the roughness at sidewalls. Therefore, it is very essential to reduce roughness by optimizing lithography and dry etching techniques for submicron SOI waveguides.

4.5 Fabrication and Measurement of Microring Resonators

SOI material is compatible with advanced CMOS processes. Specific SOI processes have been applied in microelectronics for a long

time in order to improve bulk insulation and decrease parasitic capacitances. SOI is frequently employed for optical waveguides, and the light is restricted and propagating in the top silicon layer. In this section, we will introduce the key fabrication techniques as well as the optical measurement of photonic devices.

4.5.1 Fabrication Flow

Figure 4.19 shows a typical scheme of the fabrication flow for a microring resonator. In the given scheme electron beam lithography (EBL) and dry etching (inductively coupled plasma [ICP]) are used for pattern definition. First, clean the SOI wafer. Then, spin the electron beam resist onto the wafer and bake it on a hot plate to make it hard. After that, transfer the mask pattern to the resist by EBL and etch the pattern onto the Si top layer. Remove the remaining resist, and the basic fabrication of the device is finished. Oxide cladding is often grown on the top to protect the waveguides.

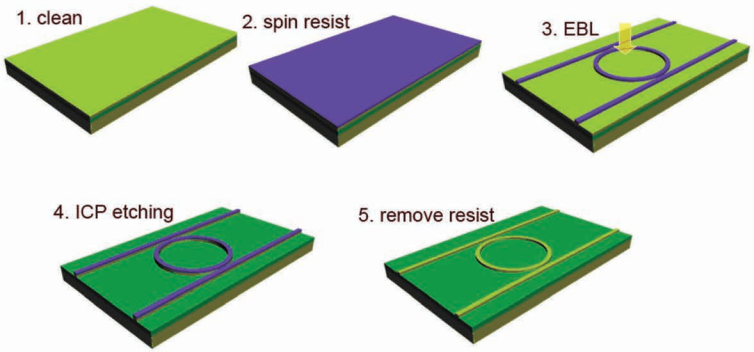

Figure 4.19 The fabrication flow of a microring resonator.

Table 4.2 lists some published processing variants and experimental results. Deep ultraviolet (DUV) lithography (commonly the krypton fluoride laser at 248 nm wavelength and the argon fluoride laser at 193 nm wavelength) and i-line lithography (365 nm wavelength from a Hg lamp) are both standard microelectronic process steps with large batch production, high speed, and low cost. On a laboratory scale, EBL and nanoimprint are flexible tools to realize optical devices of submicron dimensions.

Table 4.2 Fabrication methods for microring resonators

	Lithography	Etching	Cladding	Loss (dB/cm)	*Q* factor	FSR: nm
HKUST [17]	i-line	RIE	oxide	20	10,000	—
Ghent [18]	DUV	RIE	oxide	2.4	3000	14
IBM [19]	EBL	RIE	air	1.7	14,000	11
Cornell [20]	EBL	ICP	oxide	—	39,350	15
Purdue [21]	EBL	ICP	air	2–3	62,000	16
Aachen [22]	Nano-Imprint	RIE	air	3.5	47,700	8.3

4.5.2 Electron Beam Lithography

The wavelength of a high-energy electron wave is very short. Thus, EBL has the potential of very high resolution. EBL is widely used for scientific research due to the high accuracy. The fabrication results are mainly influenced by EB resist, proximity effect, write-field stitching error, and developing and fixing conditions.

- **Electron beam resist**

Electron beam resist belongs to polymers, chains of which can be reassembled under electron beam exposure. The exposed/unexposed region can be dissolved by a developing and fixing solution, with the mask pattern left.

- **Proximity effect**

Because of electron backscattering, electrons may spread to the near edges of adjacent patterns. And in the pattern, backscattering makes the electron density at the boundaries less than that at the center, which results in reshaping of the designed structure, as seen in Fig. 4.20a. To surpass the influence of proximity effects, pattern compensation or dose compensation methods are necessary.

- **Write-field stitching**

A large-area pattern is composed of many small write-fields for EBL. The scanning direction may be divergent from the moving direction of the sample platform, and that may result in a stitching error, as shown in Fig. 4.20b. The write-field stitching error cannot be eliminated easily, so the design would better lay important parts of patterns in a single write-field and far from the write-field borders.

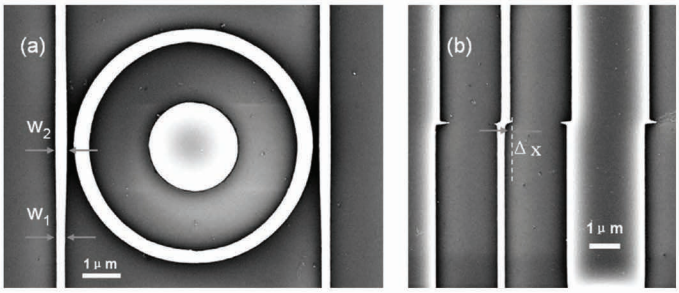

Figure 4.20 EBL: (a) proximity effect in the coupling region and (b) write-field stitching error.

- **Developing and fixing**

The dissolvability of resists changes a lot in the developer after the resists are exposed to an electron beam. Fixing is used to remove the remaining developer. The developer, fixer, and developing and fixing conditions (such as time and temperature) should be correctly chosen. Otherwise, the resist pattern misses the design targets.

4.5.3 Dry Etching Process

As an etching technique, wet etching is mostly isotropic and causes undercut. Using special solutions, wet etching can be anisotropic, but it is quite dependent on orientation. Therefore, dry etching is widely employed to fabricate submicron waveguides, which is anisotropic etching and able to get steep sidewalls.

ICP etching is a popular dry etching technique using a chemical reaction and plasma striking to remove the unprotected material, as shown in Fig. 4.21. Here, SF_6 and C_4F_8 are chosen as gases to etch silicon and passivate etching sidewalls, respectively. Both are very reactive gases that are partly ionized to a plasma by electrons accelerated under an applied voltage.

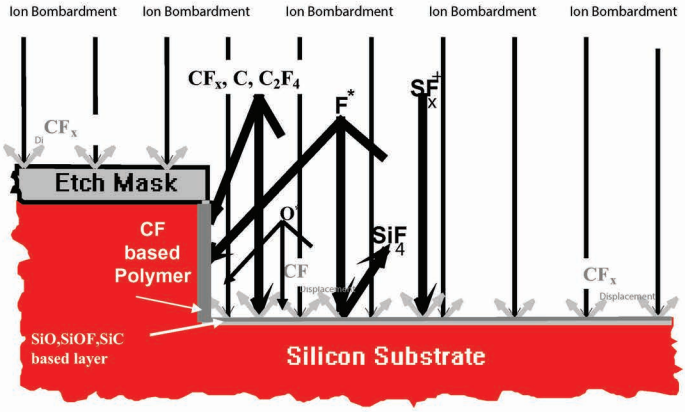

Figure 4.21 The dry etching of silicon by a plasma discharge.

The vacuum pump will extract the gas reaction products. Due to the high density of the plasma and low pressure in the ICP etching system, a high depth-to-width ratio and a high etching speed are obtained. The methods to enhance anisotropy are listed as follows:

- Increase the radio frequency (RF) power, which enhances the plasma striking, resulting in weak lateral etching.
- Lower the pressure in the reaction room, which increased the plasma free path, causing less scattering collision of the ions.
- Decrease the temperature of the sample surface, which reduces the chemical etching, as well as the lateral etching.

The RF power, pressure, constituent, and flow rate of etching gases in the reaction room play an important role in the etching process. Figure 4.22 shows the etching results of SOI-based microring resonators.

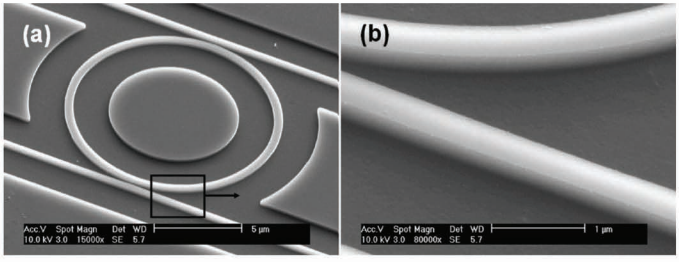

Figure 4.22 The SEM images of a microring resonator fabricated by ICP etching.

4.5.4 Silicon Oxide Growing

Thermal oxidation and chemical vapor deposition are the two main methods for silicon oxide growing. The speed of thermal oxidation is low, but this process causes less roughness and reduces optical propagation loss. SiO_2 thickness increases as the silicon is thermally oxidized. As seen in Fig. 4.23, the oxidation speed is high for juts at the boundaries of Si and SiO_2. Thus, the etching surfaces of Si are flattened after the oxide is removed. Xia et al. reduced the propagation loss in submicron SOI waveguides to 1.7 dB/cm using two-step thermal oxidation [18].

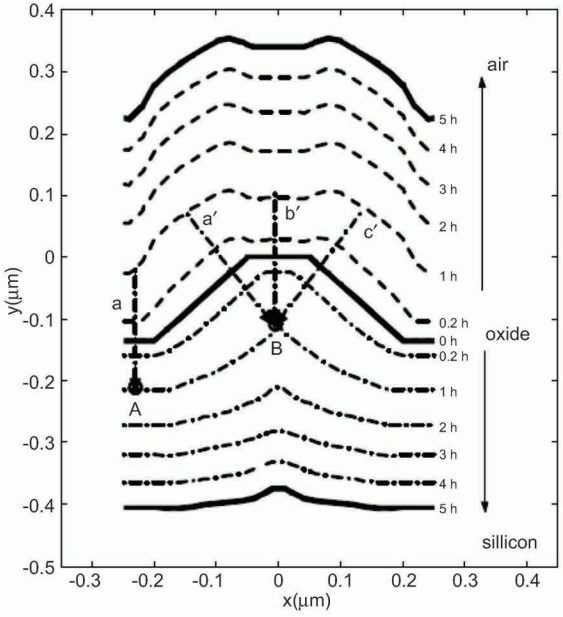

Figure 4.23 Reduction of surface roughness by thermal oxidation.

Silicon oxide can also be obtained by plasma-enhanced chemical vapor deposition (PECVD) or low-pressure chemical vapor deposition (LPCVD) with growth gases of SiH_4 and O_2. PECVD has a high deposition speed and thick oxide, while LPCVD has a dense oxide film and strong gap-filling ability. Figure 4.24 shows silicon oxide deposited by PECVD.

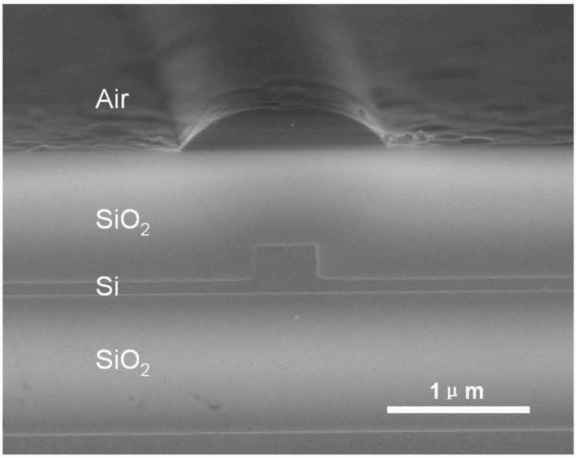

Figure 4.24 SOI waveguide with silicon oxide cladding deposited by PECVD.

4.5.5 Measurement

To measure the optical properties of microring resonators, such as filtering and time delay, we employ end fire coupling between fiber and device on the input port. A lens and a polarizer are placed behind the output port to collimate the light beam with a determined polarization, which is then focused and collected by a single-mode fiber with a collimator at the end.

- **Filtering measurement**

Figure 4.25 plots the setup for filtering measurement. The light from a frequency-tunable laser is coupled into the waveguides through a polarization controller and a polarization-maintaining fiber. The output light is collimated by a lens and then filtered by a polarizer. By turning the mirror, we can switch the collimated light either into an infrared camera or into a fiber with a collimator at the front end. With the light spot observed on the camera, we tune the measurement stages for accurate coupling. After that, the mirror is turned to lead the light to an optical spectrum analyzer (OSA) synchronously and then the transmission spectrum on the OSA is displayed.

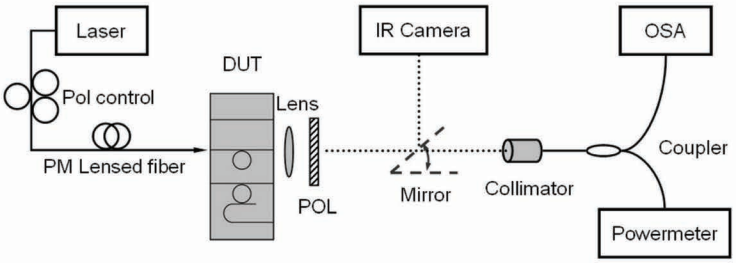

Figure 4.25 The measurement setup for microring filter characterization.

- **Time delay measurement**

As shown in Fig. 4.26, this is a setup for time delay measurement. The modulated optical signal is split into two parts, one going through the resonators and the other for reference. The main signal will be chosen to detect the optical switch at the output port. Detect and store the reference light and light from devices in oscillograph, respectively. Then, we can obtain the time delay by comparing these two waveforms.

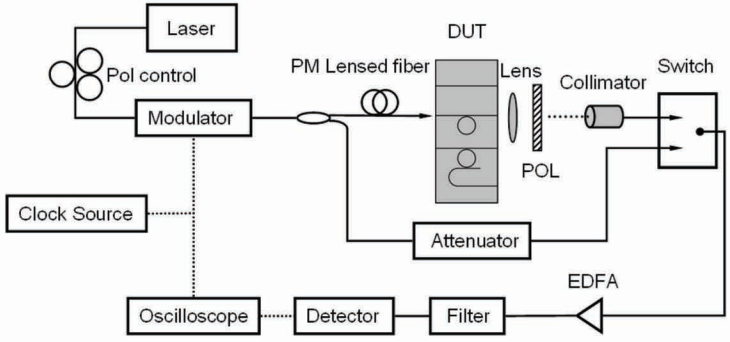

Figure 4.26 The measurement setup for time delay of microring resonators.

4.6 Applications of Microring Resonators

Microring resonators serve as building blocks in various functional components of integrated photonics. First, because of wavelength selectivity, a microring resonator can be used as an optical filter that is even tunable by thermo-optic effect or electro-optic effect. Second, the optical intensity in the microring is enhanced greatly compared to the input waveguide and, hence, the optical nonlinearity becomes

significant in the microring resonator, leading to novel devices, such as Raman lasers and optical logic devices. Third, the optical pulse is time delayed due to wave dispersion in the microring resonator, enabling optical buffers in optical interconnects. In this section, we will illustrate the applications of SOI-based microring resonators, mainly in these three aspects.

4.6.1 Optical Filter

Microring resonators are wavelength sensitive and traveling-wave resonating, which is promising for optical filtering. They can construct many kinds of filters, such as all-pass filter, add-drop filter, optical demultiplexer/multiplexer, and tunable filter.

- **All-pass filter**

The microring resonator coupled to a bus waveguide is an all-pass filter, for which the transfer function is calculated from Eq. 4.4 using Eqs. 4.69 and 4.70 for determining the transfer coefficients.

Lowering the coupling efficiency and increasing the round-trip attenuation would decrease the bandwidth of the stop-band. The extinction ratio is determined by the relation of coupling efficiency and round-trip attenuation, which achieves maximum at the critical coupling. Figure 4.27 shows the microscope image and transmission spectrum of an all-pass filter based on an SOI microring resonator [23].

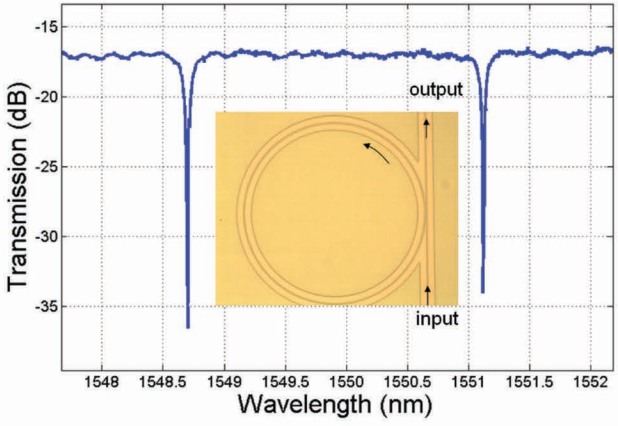

Figure 4.27 Microscope image and transmission spectrum of a an SOI-based optical filter.

Seen in Fig. 4.28, with a microring coupled to an arm, the Mach–Zehnder interferometer (MZI) can also act as an all-pass filter [24], for which the transfer function is expressed by the interference of both arms, one with and one without a coupled microring.

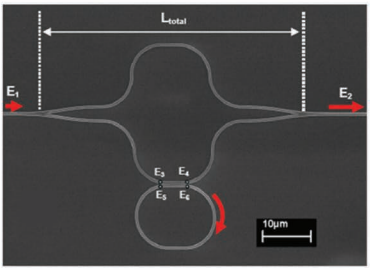

Figure 4.28 All-pass filter based on MZI coupled with a microring resonator. Reprinted with permission from Ref. [24] © The Optical Society.

The lengths of two arms are the same in the given example of Fig. 4.28. Therefore, the phase difference is 2 $m\pi$ (m is an integer) for off-resonance, while it is $(2m + 1)\pi$ for on-resonance, which causes destructive interference. The phase difference between both arms has to be considered if the arm lengths are not equal. By changing coupling efficiency, the bandwidth of the all-pass resonator may be tuned effectively.

- **Add-drop filter**

In the wavelength division multiplexing system, the add-drop filter is a key component, which adds or drops signals of special wavelengths at the network nodes. A microring resonator coupled with two bus waveguides can serve as an add-drop filter [25].

Figure 4.29 shows the SEM image and transmission spectrum of an add-drop filter based on a microring resonator. It is band-stop filtering and band-pass filtering at the throughput port and the drop port, respectively. Moreover, we find that the microring add-drop filter is polarization dependent and the transmission is quite different for TE and TM polarization. Therefore, the microring add-drop filter can be regarded as a polarization splitter, and here the splitting ratio of TE and TM polarization exceeds 20 dB.

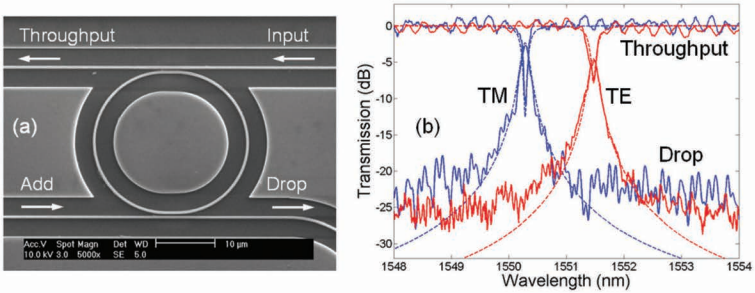

Figure 4.29 The SEM image and transmission spectrum of a microring add-drop filter. Reproduced from Ref. [25] (https://iopscience.iop.org/article/10.1088/1464-4258/11/1/015506/meta). © IOP Publishing. Reproduced with permission. All rights reserved.

The ideal response for filters is box-like, which means flat pass-band, and steep band edge. Cascades of multiple microrings in a series configuration [26], with a small footprint of only 7×10^{-4} mm^2, improve the filter response. The pass-band of five microrings is more box-like than that of three microrings and the out-of-band rejection is larger (40 dB).

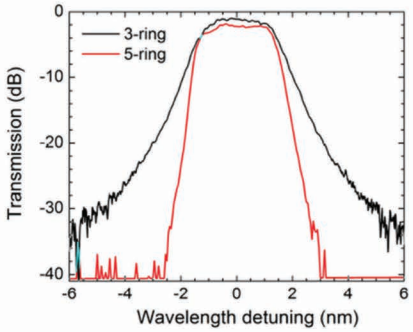

Figure 4.30 Transmission spectrum of an add-drop filter based on multiple microrings. Reprinted with permission from Ref. [26] © The Optical Society.

- **Demultiplexer/multiplexer**

A demultiplexer/multiplexer can be constructed by combining multiple add-drop filters, each corresponding to a single channel. There are several guidelines for the design. The FSR of every add-drop filter should be larger than the total bandwidth of all channels.

The spacing between adjacent two channels should be uniform. To enable low cross talk, the out-of-band rejection should be large enough for each add-drop filter.

Figure 4.31 plots an eight-channel demultiplexer in silicon [27]. The add-drop filters are based on series-coupled double microring resonators, with the drop port and the throughput port in the same direction, high out-of-band rejection, and low cross talk between channels. From the transmission, the out-of-band rejection is as large as 40 dB and the cross talk is lower than –30 dB.

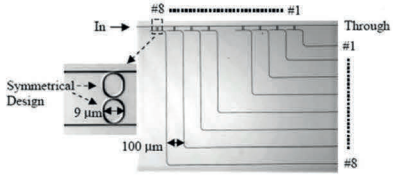

Figure 4.31 Eight-channel wavelength demultiplexer based on microring resonators. Reprinted with permission from Ref. [27] © The Optical Society.

- **Tunable filter**

A tunable filter is realizable by using a thermo-optic effect or a free carrier dispersion effect in silicon. The relation between index change and wavelength shift is described by

$$\Delta\lambda = \lambda_0 \Delta n_{\text{eff}} / n_{\text{eff}} \tag{4.74}$$

For silicon at room temperature, the thermo-optic coefficient is

$$dn/dT = 1.84 \times 10^{-4}/\text{K} \tag{4.75}$$

Thermo-optic tuning has many merits, such as fabrication simplicity, high modulation, and low power consumption, whereas the response time is limited to microsecond levels. For a high-speed response, we need to employ the free carrier dispersion effect in silicon.

At the wavelength of 1.55 μm, the index change caused by free carrier dispersion effect is

$$\Delta n = -[8.8 \times 10^{-22} \times \Delta N_{\text{e}} + 8.5 \times 10^{-18} \times (\Delta N_{\text{h}})^{0.8}], \tag{4.76}$$

where ΔN_{e} and ΔN_{h} denote the concentration changes of electron and hole in units of cm^{-3}, respectively.

The light intensity or routing will be changed when a voltage is applied. Hence, tunable filters are applicable for optical modulators/switches due to the same working mechanism. The output power spectrum is sensitive to a voltage sweep. The optical power is switched on/off within a narrow bandwidth. The speed of the modulator/switch can be increased by shortening the carrier transmitting distance and using a pre-emphasis rectangular pulse, as proposed and demonstrated by Xu et al., with a data transmission rate of 12.5 Gbit/s [28]. Using optical nonlinearity, IBM Corporation has realized all-optical switches with low bit error and a short switch time of only 2 ns [29].

4.6.2 Nonlinear Optical Devices

The optical intensity in the resonator is much larger than that in the bus waveguides. Thus, the nonlinear optical effects are enhanced, such as stimulated Raman scattering (SRS), two-photon absorption (TPA), and four-wave mixing (FWM). A centrosymmetric diamond lattice exhibits as first higher-order optical nonlinear effect the third-order susceptibility coefficients [30–32]. Second-order effects are possible with symmetry breaking structures (e.g., superlattices or strained layers).

The general Kerr effect is a change in the refractive index of a material in response to an applied electric field. John Kerr already discovered this effect in 1875 [33].The electro-optical Kerr effect is the case in which the electric field is due to the light itself. This causes a variation in the index of refraction, which is proportional to the local irradiance I of the light (I increases with the square of the electric field). The proportionality constant is called Kerr coefficient. The values of the Kerr coefficient are relatively small for most materials, on the order of 10–20 $m^2\ W^{-1}$ for typical glasses. Therefore, beam intensities on the order of 1 GW cm^{-2} (such as those produced by lasers) are necessary to produce significant variations in the refractive index via the Kerr effect. The Kerr coefficient of Si at the telecom wavelength of 1.55 μm is roughly 100 times higher (Table 4.3) than that of fiber glass [34], but the unwanted absorption increases also due to TPA. TPA increases also with the beam intensity. By convention, the proportionality is written as a product of the wavelength in vacuum times the TPA coefficient. An often-used figure of merit (FOM) relates the Kerr coefficient with

that product (wavelength*TPA coefficient). Si obtains only moderate FOM values of 0.3–0.4 at the telecom wavelength, but the FOM improves above a 2 μm wavelength because the TPA drops down at phonon energies below half of the bandgap. Unlike the situation with direct bandgap semiconductors such as GaAs, the Kerr coefficient in Si is always positive, which is assumed to be correlated with the indirect band character [35]. Many functionalities have already been demonstrated in silicon-based nonlinear devices, but often they suffer from reduced efficiency due to the rather strong TPA [36]. To overcome this limitation, alternative materials have been proposed by the scientific community, such as AlGaAs, chalcogenides, composite glasses, and nonlinear polymers in slot waveguides [34]. From the viewpoint of process integration, two materials emerged as specifically interesting, namely amorphous Si and single-crystalline SiGe [36] and graphene oxide [37].

Table 4.3 The nonlinear optical coefficients in silicon for a wavelength of 1.55 μm

	Measured
TPA coefficient	6 m/MW
Kerr coefficient	4.5×10^{-18} m^2/ W
SRS coefficient	95 m/MW

- **Raman laser**

The first silicon laser was realized through Raman effect, with a Fabry–Perot resonator. However, Fabry–Perot resonators need facet cutting, polishing, and antireflection coating, which seem to be complicated for fabrication and unsuitable for integrated photonics on chip.

Figure 4.32a shows a Raman laser based on a microring resonator. The excess free carriers are drawn out from the waveguides by a bias voltage, lowering the optical absorption. The threshold power is reduced by an order of magnitude using a microring resonator instead of a Fabry–Perot resonator. The pump efficiency and the output power both have been increased by several times with applied voltage [33], as seen in Fig. 4.32b. The Raman laser in silicon converts short wavelengths to longer wavelengths, broadening the wavelength range of the silicon laser. High-power pump lasing is done with an external laser. Hence, the application range is limited.

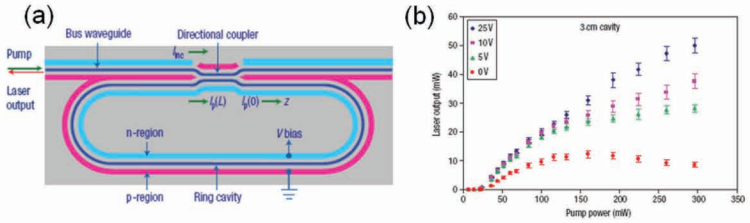

Figure 4.32 (a) The schematic image of a Raman laser and (b) output power versus pump power. Reprinted by permission from Springer Nature Customer Service Centre GmbH: Springer Nature, *Nature Photonics*, Ref. [38], copyright (2007).

- **All optical logic gates**

In terms of TPA and free carrier dispersion effect, one can realize all-optical logic gates, such as OR, AND, and NAND gates [32, 39, 40]. The microring resonator–based logic gates generally operate in this way: There are three input lights all at the resonant wavelengths: one is a signal light, and the others are control lights. The power of control lights is high, which causes optical nonlinearity and resonant peak shift of the microring resonators. If the control lights are switched, the status of the signal light will be changed, indicating optical logic operation.

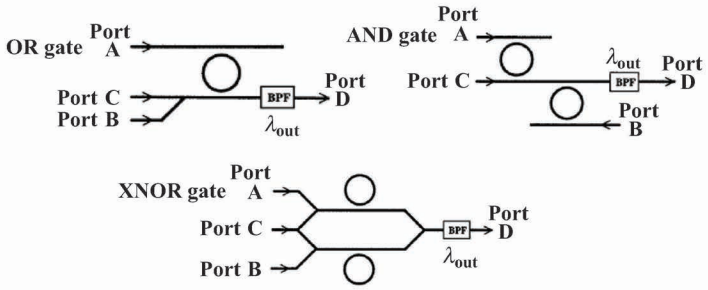

Figure 4.33 The schematics of OR, AND, and XNOR gates.

Three kinds of gates—OR, AND, and exclusive NOR (XNOR)—are presented in Fig. 4.33, where control lights are imported into A and B ports and the signal light is imported into the C port. For the OR gate, when both control lights are 0, the signal light is 0 at D, and as the control light is 1 at A or B, the resonant peaks are blue-shifted, making the signal light 1 at D. For the AND gate, just when

both control lights are 1 at A and B, the two microring resonators are resonating and the signal light is nonresonant and becomes 1 at D. For the XNOR gate, when both A and B are 0 or 1, the two arms have no phase difference, so it is 1 at D; when A or B is 1, only one microring is resonant, the phase difference is π, enabling constructive interference, and so it is 0 at D.

4.6.3 Optical Buffer

In optical interconnect and optical computing, the optical buffer plays an important role since it is able to delay optical pulses and avoid signal blocking. Microring resonators serve as time delay lines and optical buffers. When the microring is resonating, the signal light will be captured and stay in the resonator for a moment. Time delay lines based on microring resonators have such configurations as all-pass filter (APF), coupled-resonator optical waveguide (CROW), and parallel-coupled double microrings with analogue to electromagnetically induced transparency (EIT) effect [19, 36], as shown in Fig. 4.34.

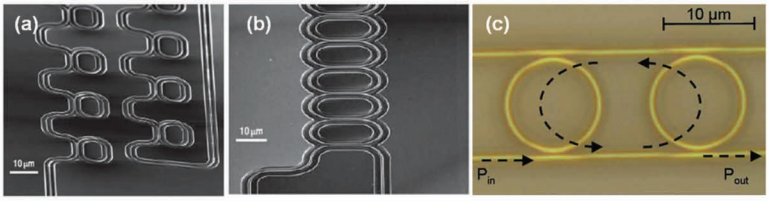

Figure 4.34 Configurations of (a) APF, (b) CROW, and (c) double microrings with analogue to EIT.

It is clear that the time delay increases with the number of cascaded microrings. However, the insertion loss increases, too. Increasing the Q factor will enlarge the delay time but decrease the bandwidth. Therefore, one should find a compromise between time delay, bandwidth, and insertion loss in the design. IBM Corporation realized a time delay of 510 ps and a 10-bit buffer, with series-coupled microring resonators with a footprint of only 0.09 mm^2. In the parallel-coupled double microrings, each ring acts as a "reflector." Thus, the two reflectors construct a "Fabry–Perot resonator" with analogue to EIT. Table 4.4 presents some results of optical buffers based on silicon microring resonators.

Table 4.4 Optical buffers based on silicon microring resonators

	Time delay (ps)	Area (mm^2)	Loss (dB)	Storage (bits)
APF of 56 rings	510	0.09	22	10 at 20 bps
CROW of 100 rings	220	0.045	23	1 at 5 bps
EIT-analogue rings	25	3×10^{-4}	4	—
Waveguides of 4 cm	500	1.13	7	>>10

4.7 Summary

Several decades have passed since the invention of microring resonators. Microring resonators have made great progress in the first decade of the 21st century because of their broad use in silicon photonics. Unlike facet mirrors and distributed Bragg reflectors, they are easily integrated in planar Si microelectronics technology and they are very versatile combined with other components, such as waveguides, mirrors, and MZIs.

There is constant progress in microring resonator design and fabrication, especially in terms of:

- Improvement in the processes to develop the performance. Industrial DUV lithography and nanoimprint lithography are employed and optimized.
- Development of novel functional photonic devices such as optical filters, modulators, switches, lasers, and logic gates.
- Application as reconfigurable wavelength routers to increase transmission bandwidth in the optical networks mainly based on point-to-point communications [37].
- Paving the way to new application fields. For example, on-chip sensors and biosensors became a strong research focus recently.

However, some inherent challenges confront microring technology and system performance, such as low processing tolerance, temperature sensitivity, and polarization dependence. Promising solution paths include (i) employing advanced techniques to increase the fabrication accuracy and optimizing the design of devices to improve the processing tolerance, (ii) introducing nanoelectronic technology and employing temperature-maintained modules to keep a stable microring resonator working, and (iii)

adding polarization converters and polarization splitters to balance the two polarizations and achieve polarization independence in system.

In summary, a microring resonator is a versatile component in integrated photonics that serves as a unit in various functional systems and plays an important role in optical communication, optical interconnect, and optical computing. With the progress in research and technology, microring resonators have become more an industrial component and find even more applications [38].

Acknowledgments

We thank Qingzhong Huang and Xi Xiao for the collection of basic information and figure drawings.

References

1. E. A. J. Marcatilli (1969). Bends in optical dielectric waveguides, *Bell Syst. Tech. J.*, **48**, 2103–2132.
2. B. E. Little, S. T. Chu, H. A. Haus, et al. (1997). Microring resonator channel dropping filters, *J. Lightwave Technol.*, **15**(6), 998–1005.
3. A. Yariv (2000). Universal relations for coupling of optical power between microresonators and dielectric waveguides, *Electron. Lett.*, **36**(4), 321–322.
4. L. Caruso and I. Montrosset (2003). Analysis of a racetrack microring resonator with MMI coupler, *J. Lightwave Technol.*, **21**(1), 206–210.
5. J. K. S. Poon, J. Scheuer, S. Mookherjea, et al. (2004). Matrix analysis of microring coupled-resonator optical waveguides, *Opt. Express*, **12**(1), 90–103.
6. S. Darmawan, Y. M. Landobasa and M. K. Chin (2007). Pole-zero dynamics of high-order ring resonator filters, *J. Lightwave Technol.*, **25**(6), 1568–1575.
7. R. Grover, P. P. Absil, T. A. Ibrahim, et al. (2004). III-V semiconductor optical micro-ring resonators, *Microresonators as Building Blocks for VLSI Photonics: International School of Quantum Electronics*, *AIP Conference Proceedings*, Vol. 709, 110–29 2004
8. Y. Yanagase, S. Suzuki, Y. Kokubun, et al. (2002). Box-like filter response and expansion of FSR by a vertically triple coupled microring resonator filter, *J. Lightwave Technol.*, **20**(8), 1525–1529.

9. J. Heebner, R. Grover and T. Ibrahiml (2007). *Optical Microresonators: Theory, Fabrication, and Applications* (Springer-Verlag, Berlin).
10. Q. Z. Huang, Y. D. Yu and J. Z. Yu (2009). Experimental investigation on submicron rib waveguide microring/racetrack resonators in silicon-on-insulator, *Opt. Commun.*, **282**, 22–26.
11. T. Barwicz, M. R. Watts, M. A. Popovic, et al. (2007). Polarization-transparent microphotonic devices in the strong confinement limit, *Nat. Photonics*, **1**(1), 57–60.
12. X. Yan, C. S. Ma, Y. Z. Xu, et al. (2005). Characteristics of vertical bent coupling between straight and curved rectangular optical waveguides, *Optik,* **116**(8), 397–403.
13. D. Marcuse (1972). *Light Transmission Optics*, 2nd ed. (Van Nostrand Reinhold, New York).
14. V. Subramaniam, G. N. DeBrabander, D. H. Naghski, et al. (1997). Measurement of mode field profiles and bending and transition losses in curved optical channel waveguides, *J. Lightwave Technol.*, **15**(6), 990–997.
15. K. K. Lee, D. R. Lim, H. C. Luan, et al. (2000). Effect of size and roughness on light transmission in a Si/SiO2 waveguide: experiments and model, *Appl. Phys. Lett.*, **77**(11), 1617–1619.
16. P. K. Tien (1971). Light waves in thin films and integrated optics, *Appl. Opt.*, **10**(11), 2395.
17. S. M. Zheng, H. Chen and A. W. Poon (2006). Microring-resonator cross-connect filters-in silicon nitride: rib waveguide dimensions dependence, *J. Sel. Topics Quantum Electron.*, **12**(6), 1380–1387.
18. P. Dumon, W. Bogaerts, V. Wiaux, et al. (2004). Low-loss SOI photonic wires and ring resonators fabricated with deep UV lithography, *IEEE Photonics Technol. Lett.*, **16**(5), 1328–1330.
19. F. N. Xia, L. Sekaric and Y, Vlasov (2007). Ultracompact optical buffers on a silicon chip, *Nat. Photonics*, **1**(1), 65–71.
20. Q. F. Xu, B. Schmidt, S. Pradhan, et al. (2005). Micrometre-scale silicon electro-optic modulator, *Nature*, **435**(7040), 325–327.
21. S. J. Xiao, M. H. Khan, H. Shen, et al. (2007). Compact silicon microring resonators with ultra-low propagation loss in the C band, *Opt. Express*, **15**, 14467–14475.
22. U. Plachetka, N. Koo, T. Wahlbrink, et al. (2008). Fabrication of photonic ring resonator device in silicon waveguide technology using soft UV-nanoimprint lithography, *IEEE Photonics Technol. Lett.*, **20**(5–8), 490–492.

23. Q. Z. Huang, J. Z. Yu, S. W. Chen, et al. (2008). Design, fabrication and characterization of a high-performance microring resonator in silicon-on-insulator, *Chinese Phys. B*, **17**(7), 2562–2566.

24. F. N. Xia, L. Sekaric and Y. A. Vlasov (2006). Mode conversion losses in silicon-on-insulator photonic wire based racetrack resonators, *Opt. Express*, **14**(9), 3872–3886.

25. Q. Z. Huang, Y. D. Yu and J. Z. Yu (2009). Design and realization of a microracetrack resonator based polarization splitter in silicon-on-insulator, *J. Opt. A: Pure Appl. Opt.*, **11**, 015506.

26. F. N. Xia, M. Rooks, L. Sekaric, et al. (2007). Ultra-compact high order ring resonator filters using submicron silicon photonic wires for on-chip optical interconnects, *Opt. Express*, **15**, 11934–11941.

27. S. Xiao, M. H. Khan, H. Shen, et al. (2007). Multiple-channel silicon micro-resonator based filters for WDM applications, *Opt. Express*, **15**(12), 7489–7498.

28. Q. F. Xu, S. Manipatruni, B. Schmidt, et al. (2007). 12.5 Gbit/s carrier-injection-based silicon micro-ring silicon modulators, *Opt. Express*, **15**(2), 430–436.

29. Y. Vlasov, W. M. J. Green and F. Xia (2008). High-throughput silicon nanophotonic wavelength-insensitive switch for on-chip optical networks, *Nat. Photonics*, **2**(4), 242–246.

30. O. Lin, O. J. Painter and G. P. Agarwal (2007). Nonlinear optical phenomena in silicon waveguides: modeling and applications, *Opt. Express*, **15**, 16606.

31. L. Zhang, A. M. Agarwal, L. C. Kimerling and J. Michel (2014). Nonlinear group IV photonics based on silicon and germanium: from near-infrared to mid-infrared, *Nanophotonics*, **3**, 247–268.

32. H. K. Tsang and Y. Liu (2008). Nonlinear optical properties of silicon waveguides, *Semicond. Sci. Technol.*, **23**(6), 064007.

33. J. Kerr (1875). A new relation between electricity and light:Dielectric media birefringent, *Phil. Mag.*, **50**(332), 337–348.

34. J. Leuthold, C. Koos and W. Freude (2010). Nonlinear silicon photonics, *Nat. Photon.*, **4**, 535–544.

35. M. Dinu, F. Quochi and H. Garcia (2003). Third-order nonlinearities in silicon at telecom wavelengths, *Appl. Phys. Lett.*, **82**, 2954–2956.

36. C. Lacava, M. A. Ettabib and P. Petropoulos (2017). Nonlinear silicon photonic signal processing devices for future optical networks, *Appl. Sci.*, **7**, 103.

37. X. Xu et. al. (2017). Observation of third-order nonlinearities in graphene oxide film at telecommunication wavelength, *Sci. Rep.*, **7**, 9646.

38. H. S. Rong, S. B. Xu, Y. H. Kuo, et al. (2007). Low-threshold continuous-wave Raman silicon laser, *Nat. Photonics*, **1**(4), 232–237.

39. T. A. Ibrahim, K. Amarnath, L. C. Kuo, et al. (2004). Photonic logic NOR gate based on two symmetric microring resonators, *Opt. Lett.*, **29**(23), 2779–2781.

40. T. A. Ibrahim, R. Grover, L. C. Kuo, et al. (2003). All-optical AND/NAND logic gates using semiconductor microresonators, *IEEE Photonics Technol. Lett.*, **15**(10), 1422–1424.

41. Q. F. Xu, J. Shakya and M. Lipson (2006). Direct measurement of tunable optical delays on chip analogue to electromagnetically induced transparency, *Opt. Express*, **14**(14), 6463–6468.

42. J. Thomson, F. Y. Gardens, J.-M. Fédéli, S. Zlatanovic, Y. Hu, B. P. P. Kuo, E. Myslivets, N. Alic, S. Radic, G. Z. Mashanovich and G. Reed (2012). 50-Gb/s silicon optical modulator, *IEEE Photon. Technol. Lett.*, **24**(4), 234–236.

43. M. Calvo et. al. (2019). Ring resonator designed for biosensing applications manufactured on 300 mm SOI in an industrial environment, *Jpn. J. Appl. Phys.*, **58**, SBBE02.